RSC Advances

PAPER

View Article Online
View Journal | View Issue

Cite this: *RSC Adv.*, 2024, **14**, 33977

Preparation of biochar/iron mineral composites and their adsorption of methyl orange

Yaqiong Dong,[ad] Jianjun Liang,[abc] Zhengyang E,[ad] Jiayu Song,[ad] Changjie Liu,[ac] Zhe Ding,[ac] Wei Wang[ac] and Wentao Zhang *[ac]

Biochar-supported iron-containing minerals have received much attention due to their synergistic mechanism of decontamination in environmental pollution remediation. In this work, two types of iron/biochar were prepared from different biomasses using ferric chloride as the Fe source and rice husks and peanut shell as biomasses. The formation of fayalite (Fe_2SiO_4) and magnetite (Fe_3O_4) in rice husk and peanut shell derived biochar was proved by X-ray diffraction. These minerals not only optimized the physicochemical properties of the biochar but also enhanced its capacity to adsorb methyl orange (MO). Peanut shell-based biochar (PBC) and rice husk-based biochar (RBC) sequestered 3.9 mg g^{-1} and 4.5 mg g^{-1} of MO, respectively. In contrast, iron peanut shell-based biochar (Fe-PBC) and iron rice husk-based biochar (Fe-RBC) adsorbed 6.0 mg g^{-1} and 17.2 mg g^{-1}, outperforming their pristine biochar. The removal of MO showed a synergistic effect due to the loading of iron-bearing minerals. The mechanisms of MO immobilization by biochar samples were explored by experimental and characterization methods. It was found that the mechanisms responsible for MO immobilization on composites were conducted by electrostatic attraction, complexation with oxygen-containing functional groups, π–π interaction and hydrogen bond formation. This finding clarified the relationship among biomass composition, iron mineral evolution, and the adsorption capacity of iron-modified biochar, which is essential for the development of a cost-effective adsorbent.

Received 30th July 2024
Accepted 10th October 2024

DOI: 10.1039/d4ra05529b

rsc.li/rsc-advances

1 Introduction

Environmental contamination has been a major issue in the world, which causes a severe threat to food safety, human health, and ecosystem stability.[1–3] There have been increasing calls for sustainable solutions to environmental issues. Exploring cost-effective remediation materials has become an urgent subject for both academic and industrial communities.[4–7] Biochar has garnered significant interest because of its cheap and convenient sources, high porosity, large surface area, abundant functional groups, and excellent adsorption properties.[8–10] It has found wide applications in various fields, including carbon sequestration,[11] soil amendment[12] and wastewater treatment.[13] Consequently, numerous biochar-based adsorbents were designed and employed to successfully remove pollutants.[2] As a wastewater adsorbent, biochar is increasingly acknowledged as an alternative to activated carbon (AC) for the removal of various contaminants, including inorganic anions (NO_3^-, PO_4^{3-}), metal cations (Pb(II), As(III) and Cd(II)), organic dyes (crystal violet, cationic red X-GRL), *etc.*[14,15] Nevertheless, its relatively low surface area and susceptibility to abiotic and/or biotic processes may limit its effectiveness in certain applications.[16]

The widespread adoption of engineered biochar has significantly enhanced its performance.[17,18] Various modifications have been attempted, including physical, chemical, mineral impregnation, and magnetic modifications.[19–22] In recent years, loading metal onto biochar has garnered widespread attention due to its excellent performance in the removal of metal ions and organic substances.[3,13,23,24] Among abundant reports on metal-modified biochar,[14–17] iron was often chosen due to its low price and superior surface adsorption properties.[25–27] It has been reported that the composite of biochar and iron oxides (such as magnetite and hematite) could exhibit high synergistic adsorption performance of organic matter and wide application in environmental remediation.[17,28,29] For example, incorporating iron compounds into biochar increases its surface area and creates additional contact points, like Fe–O bonds, enhancing its adsorption ability.[30] It is reported that the maximum adsorption capacity of iron/biochar for arsenic was approximately twice of biochar.[31] Iron/biochar is valuable for its outstanding pollutant removal performance. However, many studies have only focused on the structural construction and

[a]*Northwest Institute of Eco-Environment and Resources, Chinese Academy of Sciences, Lanzhou 730000, China. E-mail: gslzwtao@sina.com*

[b]*Key Laboratory of Strategic Mineral Resources of the Upper Yellow River, Ministry of Natural Resources, Lanzhou 730046, China*

[c]*Key Laboratory of Petroleum Resources Exploration and Evaluation, Lanzhou 730000, Gansu Province, China*

[d]*University of Chinese Academy of Sciences, Beijing 100049, China*

application of a single type of iron/biochar. In-depth research into whether and how biomass types affect the structure and performance of iron/biochar has been lacking.

Numerous studies have confirmed that biomass feedstocks and compositional differences significantly influence the physicochemical properties and performance of biochar.[32–34] For instance, biochar derived from woody and herbaceous biomass exhibits significant differences in yields, specific surface areas, element compositions, and adsorption capacities. The interaction between biomass and minerals such as iron and clay, can influence the degree of aromatic condensation, the concentration of acidic functionalities, and the porosity of biochar during pyrolysis. These factors ultimately determine the stability and adsorption performances of biochar.[35] However, it remains unclear how biomass with different compositions and structures affects the formation of iron compounds when loaded with various iron salts. At the same time, unfortunately, most studies on the removal of pollutants by iron-based biochar only focus on the adsorption process of pollutants. In fact, the adsorption sites of organic pollutants at the interface of the composites are also worth exploring due to the different bond structure between iron and biochar.

The annual production of rice husk and peanut shells, which are the main agricultural solid waste by-products in China, is estimated to be 4.4 million tones and 3.14 million tones, respectively.[36–38] Rice husk contains approximately 40% cellulose, 30% lignin, and the remaining 20% consists of silica, adsorbed water, alkaline minerals, and other trace elements.[39] In contrast, peanut shell is composed of 94.0% organic matter, 41.08% cellulose, 25.30% hemicellulose, 29.54% lignin, and 3.4% ash.[40] The significant differences in the structure and composition of these two biomasses will result in distinct structures and properties of the prepared biochar. Therefore, rice husk and peanut shell were selected in this study as biomass resources for biochar production. Methyl orange (MO) is a common water-soluble azo anionic dye and pH indicator widely used in the textile industry. MO contains aromatic and –N=N– groups, making it highly toxic, carcinogenic, teratogenic, and harmful to the environment and organisms.[41,42] Thus, MO is identified as a potential organic pollutant that requires proper treatment before discharge into natural water bodies.

In this study, we collect two kinds of biomass (rice husk and peanut shell) combined with ferric chloride to prepare two types of iron/biochar, which were subsequently used for the removal of MO. The objectives of this study were fourfold (1) to use characterization techniques to evaluate the effects of biomass types on the structural properties and iron fractions in biochar derived from rice husk and peanut shell; (2) to assess the efficacy of the different iron-modified biochar in removing MO; (3) to propose the main removal mechanism for MO; and (4) to explore key factors influencing MO removal by different biochar. Our findings provide insights into the correlation among biomass composition, the evolution of iron minerals, and the adsorption capacity of iron-modified biochar. Furthermore, we also established a solid foundation for utilizing waste resources and the treating of dye pollution.

2 Materials and methods

2.1 Chemicals and materials

Peanut shells and rice husks were obtained from Henan Province, China. All the biomasses were rinsed several times using deionized water (DI water, 18.2 MΩ cm^{-1}) to remove surface dirt. These biomass samples were then dried at 60 °C for 24 h, and crushed into powders using a pulverizer. All reagents, including ferric chloride hexahydrate ($FeCl_3 \cdot 6H_2O$) and MO, were purchased from Energy Chemical. All chemical reagents were of analytical grade and used without further purification.

2.2 Biomass modification

Peanut shell and rice husk powders were modified by adding 20.0 g biomass to 150.0 mL of 81.1 g L^{-1} $FeCl_3$ solution under intermittent ultrasound with ice bags for 36 h, followed by stirring the mixture at 500 rpm for 24 h. The obtained mixture was sealed into a beaker, and a change in color indicated the production of the composite materials. The solid was obtained by centrifugation at 5000 rpm for 15 min. The product was oven-dried at 80 °C for 48 h. Finally, the lumpy sample was ground into fine particles for further use.

2.3 Preparation of biochar

Biochar was fabricated by the co-pyrolysis method.[43] Briefly, peanut shell powder, rice husk powder, and their respective iron-modified powders were individually placed into a tube furnace. The temperature was increased to 800 °C at a rate of 5 °C min^{-1} and held at 800 °C for 3 h under a nitrogen atmosphere. The final residue was rapidly cooled and then milled to obtain powdered samples, designated as peanut shell-based biochar (PBC), rice husk-based biochar (RBC), iron peanut shell-based biochar (Fe-PBC), and iron rice husk-based biochar (Fe-RBC), respectively. The obtained products were washed with deionized water four times, freeze-dried, and passed through a 200-mesh sieve to obtain uniform biochar powder.

2.4 Characterization

Fourier-transformed infrared spectroscopy (FT-IR, Bruker Vertex70, Germany) was used to qualitatively measure the functional group composition of the biochar surface. A scanning region of 400–4000 cm^{-1} was recorded with a resolution of 4 cm^{-1} and 64 scans. X-ray diffraction (XRD) patterns were carried out on an X-ray diffractometer (XD-3A, Shimadzu, Japan) with Bragg–Brentano geometry for 2θ values in a range of 5–90°. N_2 gas adsorption and desorption analyses were carried out using Brunner–Emmett–Teller (BET) analyzer (ASAP2020, Micromeritics Corp., USA) at a constant temperature (−196 °C). The dry samples were pretreated for 6 h at 110 °C under N_2 atmosphere to remove any surface water or gas. The surface area of samples was calculated using the BET method. The surface morphology analysis was observed using a scanning electron microscope (SEM, S-4800, Hitachi, Japan). The surface electrochemical properties and zeta potential of the sample materials were determined *via* the Malvern Instrument Zeta-Sizer Nano ZS

(Malvern Instruments Co. Ltd., UK). The elemental information analysis was characterized using X-ray photoelectron spectroscopy (XPS, ESCALAB 250XI, Thermo Scientific) with Al-Kα radiation. All spectra were calibrated to the C 1s peak at 284.6 eV. The effects of pH and initial concentration of MO on its removal, as well as the zeta potential of biochar samples at different pH levels, were expressed as mean ± standard deviation ($n = 3$). The Microsoft Office Excel 2010 was used to analysis experimental data. Pearson linear correlation analysis was used to investigate the relationships among the data ($p < 0.05$) by SPSS 25. All figures were produced by Origin Pro (2018).

2.5 Adsorption experiments

All batch experiments for MO removal were performed on a batch thermostatic shaker. In general, 50 mg biochar was added to a 75 mL conical flask containing 50 mL of 20 mg L^{-1} MO solution. The flask was then placed on a shaker and shaken at 180 rpm for 27 h under ambient conditions. The initial pH of the solution was controlled at pH ~ 6.0 by using 0.1 mol L^{-1} HCl and 0.1 mol L^{-1} NaOH solutions. The pH edge tests were conducted within a pH range of 3.1 to 9.6.

The kinetics studies were conducted to measure the time-dependent adsorption of MO on representative materials. The studies were carried out in 75 mL conical flasks containing 50 mL adsorbent solutions with an initial MO concentration of 20 mg L^{-1}. To each flask, 50 mg adsorbent was added, and equilibration was reached in a shaker at predetermined time intervals under ambient temperature conditions.

The concentrations of MO in the solution were determined by UV-vis spectrophotometer at maximum absorbance (λ_{max} = 464 nm). The adsorption amount of MO on biochar (q_e, mg g^{-1}) was calculated by using the below equation (eqn (1)):

$$q_e = \frac{(C_i - C_e) \times V}{m_b} \quad (1)$$

where C_i and C_e were MO concentrations (mg L^{-1}) in solution at t_i and t_e, respectively. V was the solution volume (L), and m_b is the mass of the adsorbent used (g).[44]

The adsorption kinetics were analyzed by pseudo-first-order and pseudo-second-order kinetic models. The linear forms of pseudo-first-order and pseudo-second-order kinetic models are shown in eqn (2) and (3), respectively.

$$\ln(q_e - q_t) = \ln q_e - k_1 t \quad (2)$$

$$\frac{t}{q_t} = \frac{1}{k_2 q_e^2} + \frac{t}{q_e} \quad (3)$$

where q_t was the adsorption amounts (mg g^{-1}) of the adsorbate at time t (min). k_1 (min^{-1}) and k_2 (g (mg^{-1} min^{-1})) were the rate constants, respectively.[45]

3 Results and discussion

3.1 Characterization of biochar

As depicted in Fig. 1a and b, PBC displayed a smooth surface with minor pore structures, while RBC exhibited a rough surface morphology with voids and grooves. The surface of Fe-PBC was covered with small, sharp, conical particles, which were stacked to form numerous gaps and holes (Fig. 1c). However, the surface of Fe-RBC exhibited finer cracks, holes, and smaller particles that were densely arranged in clusters (Fig. 1d). Fig. 1e and f displayed the distribution of iron on the surfaces of Fe-RBC and Fe-PBC. This distribution resulted from the tendency of surface-adsorbed Fe^{3+} to form iron-containing minerals during pyrolysis, which then aggregate into clusters on the biochar.[29,46] XRD patterns of Fe-PBC and Fe-RBC were presented in Fig. 1g and h. The XRD pattern of Fe-PBC showed the main diffraction peaks located at 2θ = 29.5°, 35.1°, 42.4°, 56.0° and 72.7°, indicating that the iron species loaded on PBC surface mainly in the form of magnetite (Fe_3O_4) (PDF #19-0929). For Fe-RBC, the main diffraction peaks located at 25.0°, 31.5°, 34.8°, 35.8°, and 51.3°, which could be assigned to fayalite (Fe_2SiO_4) (PDF #34-0178). The XRD spectra showed that the biomass significantly influenced the type of iron-bearing minerals present in the biochar.

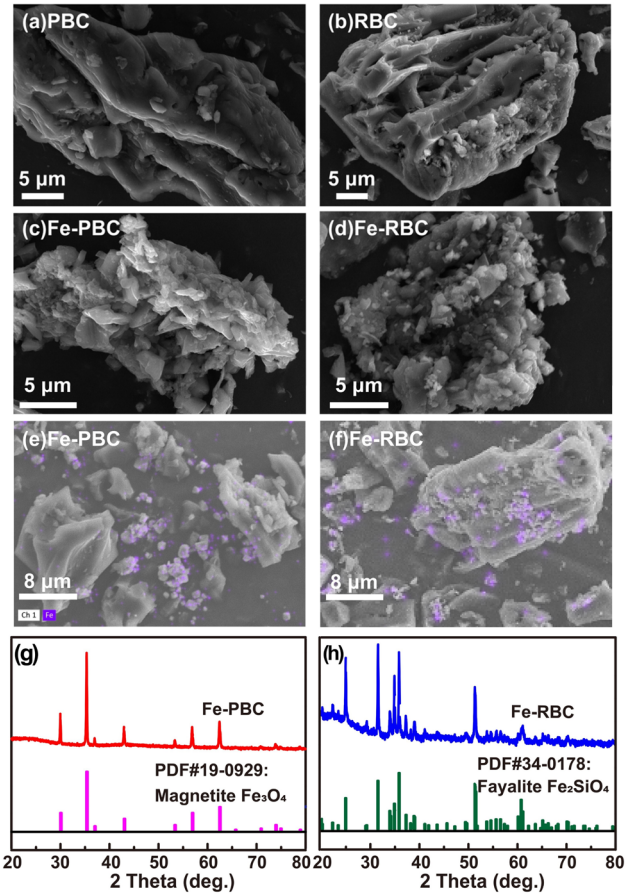

Fig. 1 SEM images of (a) PBC, (b) RBC, (c) Fe-PBC and (d) Fe-RBC. The iron distribution of (e) Fe-PBC and (f) Fe-RBC. XRD patterns of (g) Fe-PBC and (h) Fe-RBC.

FT-IR spectra of biochar samples were illustrated in Fig. 2a. Both PBC and RBC were rich in oxygen-containing functional groups including OH, C=O, C–O–C, and O=C–O.[45] It was evident that RBC exhibited a distinct vibration at 471 cm^{-1}, corresponding to ν(Si–O),[4] whereas this peak was absent in PBC.

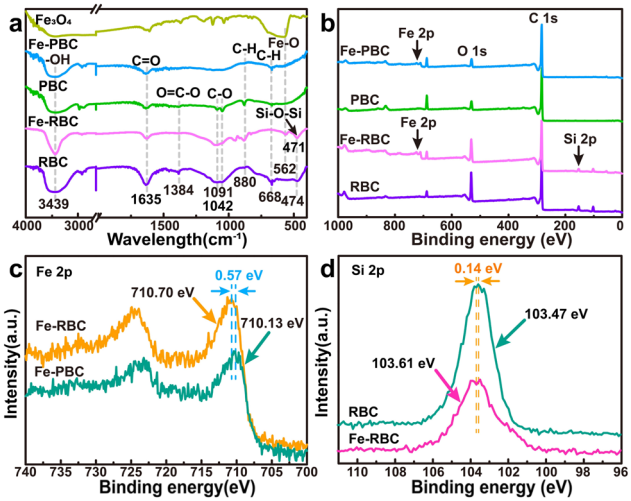

Fig. 2 (a) FT-IR spectra and (b) XPS survey of all samples. High-resolution of (c) Fe 2p and (d) Si 2p XPS spectra of pristine biochar and iron-modified biochar.

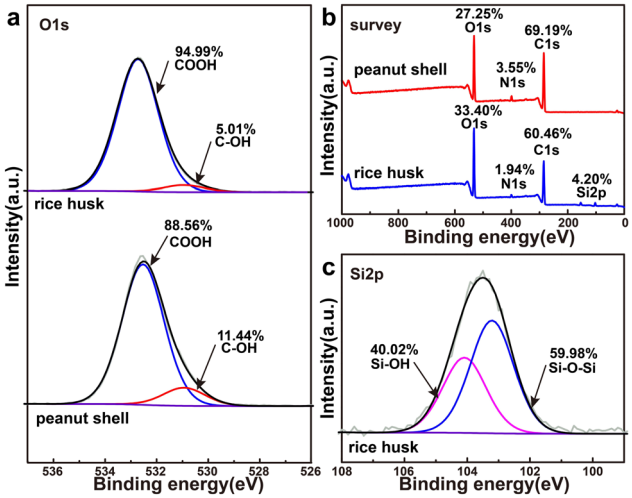

Fig. 3 XPS spectra of (a) O 1s, (b) survey and (c) Si 2p of rice husk and peanut shell.

The successful loading of iron-containing minerals was confirmed by the presence of characteristic bands at 562 cm^{-1}, corresponding to Fe–O stretching vibrations.[47] After pyrolysis, the position of the Si–O peak (471 cm^{-1}) in PBC shifted to 474 cm^{-1} for Fe-PBC, indicating a change in the chemical environment of Si–O. The introduction of iron-supporting minerals reduced the peak intensity of pristine biochar in the FT-IR spectra of PBC and RBC.[30]

As shown in Fig. 2c, the XPS spectra of Fe 2p indicated that the major binding energy in Fe-RBC (710.60 eV) was notably higher than that in Fe-PBC (710.13 eV). This difference could be attributed to the presence of different iron-bearing minerals in the prepared samples.[48] The XPS spectra of Si 2p (Fig. 2d) revealed a shift in the main peak position for Fe-RBC compared to RBC, with the peak moving to a higher energy by 0.14 eV. This result further confirms the transformation of the chemical form of silicon during the pyrolysis of iron-containing biomass.[4] After the formation of iron-containing minerals in biochar, the metal–oxygen bonds and oxygen-containing functional groups on the surface of biochar may play a major role in removing MO.[49]

The XPS survey (Fig. 2b and Table 1) indicated that the main constituent elements were consistent in both PBC and RBC. However, the most notable difference was that RBC contains about 7% silicon, whereas no silicon was detected in PBC. In addition, the differences in silica-containing species in biochar can be attributed to variations in the elemental composition of the biomass used to prepare biochar. Table 1 shows that rice husk contains silicon at a level similar to that found in RBC. We speculated that silicon in rice husk, along with Fe^{3+} adsorbed on the surface can combine to form Fe_2SiO_4 during pyrolysis.[49,50]

Table 1 Elemental contents of samples based on XPS survey

Content (%)	C	N	O	Si	Fe
Peanut shell	69.20	3.55	27.25	—	—
Rice husk	60.46	1.94	33.40	4.20	—
PBC	91.25	1.26	7.49	—	—
Fe-PBC	90.97	1.04	6.46	—	1.53
RBC	74.24	1.08	17.68	7.00	—
Fe-RBC	76.65	1.36	15.22	4.64	2.13

According to Fig. 3b and Table 1, the Fe content in Fe-PBC was 1.53%, apparently lower than that in Fe-RBC (2.13%). This disparity may be attributed to the different oxygen contents in the two biomasses. As shown in Table 1, rice husks exhibited higher oxygen content (33.40%) than peanut shells (27.25%). As shown in Fig. 3a and Table 1, rice husks contained more COOH groups (94.99%) than peanut shells (88.56%), which could enhance their affinity with Fe^{3+}.[48] Therefore, the iron loading on Fe-RBC was greater than Fe-PBC. Moreover, Fig. 3b and Table 1 showed that the nitrogen content in peanut shells (3.55%) was higher than in rice husk (1.94%). However, increasing the nitrogen content does not alter the mineral structure of Fe in PBC.

Therefore, the differences in iron-containing minerals on the iron/biochar surface have two main sources. First, the difference in total iron contents of the feedstocks during impregnation was caused by variations in the oxygen content of different biomasses, with the COOH content being the primary factor. Second, the silicon content of the biomass plays a crucial role in controlling the formation of iron minerals during the pyrolysis process.

According to the IUPAC classification, RBC, PBC, and Fe-PBC displayed the mixture of reversible Type I and Type II adsorption isotherms, indicating that the porous network was composed of micropores and mesopores.[51,52] In addition, hysteresis loops characteristic of the H4 type were observed in RBC, PBC, and Fe-PBC, where mesopores are primarily composed of narrow slit pores.[53] However, Fe-RBC exhibited Type II isotherms with H3 hysteresis loops, indicating the presence of both micro- and mesopores in its pore structure,

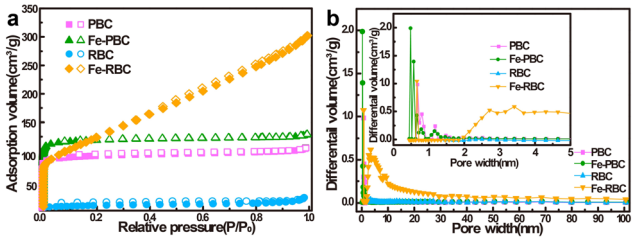

Fig. 4 (a) Nitrogen adsorption–desorption isotherms and (b) pore size distributions based on desorption branches of PBC, RBC, Fe-PBC, and Fe-RBC.

Table 2 Statistical table of porosity and specific surface area of different samples

Biochar	Surface area ($m^2\ g^{-1}$)	Average pore size (nm)	Pore volume ($cm^3\ g^{-1}$)
RBC	25.3	5.04	0.03
Fe-RBC	455.5	4.11	0.47
PBC	277.0	2.34	0.16
Fe-PBC	359.0	2.23	0.20

along with a higher mesopore content compared to other biochar.[54,55] The specific surface areas of iron/biochar were 455.5 $m^2\ g^{-1}$ for Fe-RBC and 359.0 $m^2\ g^{-1}$ for Fe-PBC, which were 18.0 and 1.3 times higher than those of RBC (25.3 $m^2\ g^{-1}$) and PBC (277.0 $m^2\ g^{-1}$), respectively (Fig. 4a and Table 2). This probably due to the attachment of iron oxide on biochar surface[56] to the dispersion of iron-containing minerals in specific regions on the biochar.[49,57] The SEM test results also proved this result. There was a significant increase in pore volume for RBC and Fe-RBC (from 0.03 to 0.47 $cm^3\ g^{-1}$), and also from 0.16 to 0.20 $cm^3\ g^{-1}$ for PBC and Fe-PBC. The increase in pore size of iron/biochar was mainly attributed to the corrosion of carbon structure during pyrolysis of Fe^{3+} impregnating biomass and the contribution of reaction gas to the pore formation.[49,58] The alternation of surface areas may affect the sorption ability of biochar for organic pollutants immobilization.[59,60]

3.2 Adsorption kinetics

As shown in Fig. 5a and b, the adsorption process could be divided into two stages: (1) a rapid adsorption stage from 0 to 50 min, and (2) a slower adsorption stage after 50 min. The adsorption of MO on Fe-RBC was rapid, reaching 84.3% within 50 min. The adsorption of Fe-RBC was 14.5 mg g^{-1}, and approximately 3.6, 3.8, and 5.0 times higher than that of Fe-PBC, RBC, and PBC, respectively. Adsorption equilibrium was reached within approximately 27 h, with Fe-RBC exhibiting an adsorption capacity of 17.2 mg g^{-1}. Adsorption kinetic modeling described the transfer of MO from solution to the solid adsorbent,[61] with the observed data fitted to pseudo first-order and second-order kinetic models. The relevant kinetic parameters were listed in Table 3, and the plots were shown in Fig. 5c and d. The pseudo second-order model, with a higher R^2

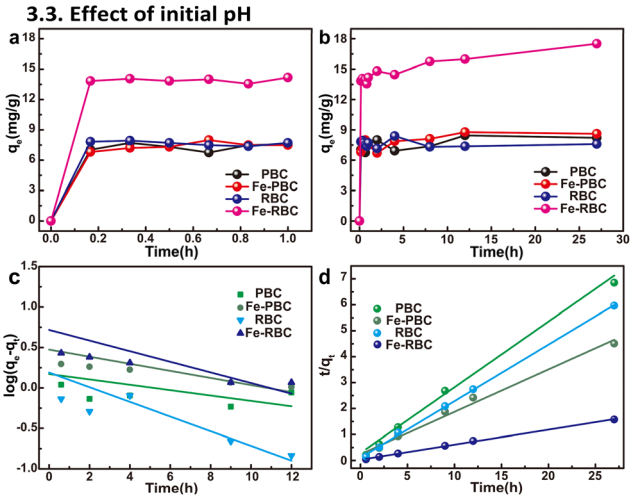

Fig. 5 (a) and (b) Adsorption kinetics, (c) pseudo-first-order fits, (d) pseudo-second-order fits on MO removal in PBC, RBC, Fe-PBC, and Fe-RBC systems. Biochar dose = 1.0 g L^{-1}, $[MO]_0$ = 20 mg L^{-1}, initial pH = 6.0 ± 0.1, and T = 25 °C.

Table 3 The kinetics parameters for the adsorption of MO by biochar

	Pseudo-first-order		Pseudo-second-order	
Biochar	k_1 (min^{-1})	R^2	k_2 (g ($mg^{-1}\ min^{-1}$))	R^2
RBC	−0.063	0.641	0.218	0.999
Fe-RBC	−0.035	0.442	0.058	0.999
PBC	−0.008	0.122	0.253	0.979
Fe-PBC	−0.026	0.525	0.164	0.987

value, better described the adsorption process than the pseudo first-order model.

As indicated in Fig. 6a, the adsorption of MO increased with the increase of the initial concentration of MO. At the highest MO concentration, the maximum adsorption of the four kinds of biochar followed the order of Fe-RBC (17.2 mg g^{-1}) ≫ Fe-PBC (6.0 mg g^{-1}) > RBC (4.5 mg g^{-1}) > PBC (3.9 mg g^{-1}). Among these biochar samples, the affinity and removal rates of all iron/biochar composites for MO were higher than those of pristine biochar.

3.3 Effect of initial pH

The initial pH influences the surface properties of the biochar samples and the form of MO, which will, in turn, affect the adsorption process of MO.[62] As shown in Fig. 6b, the results indicate that the adsorption of MO on biochar samples gradually decreased with increasing pH values ($p < 0.05$). At pH ~3.0, the adsorption of MO on biochar reached the maximum, which indicates that MO adsorption on biochar was favored under acid conditions. In particular, the adsorption of MO on Fe-RBC was up to 18.3 mg g^{-1} at pH ~3.0, and decreased to 13.6 mg g^{-1} at pH ~9.6. Such phenomena could be attributed to the electrostatic attraction between MO molecules and biochar surface (Fig. 6b). As is well known, MO molecules contain sulfonate (–

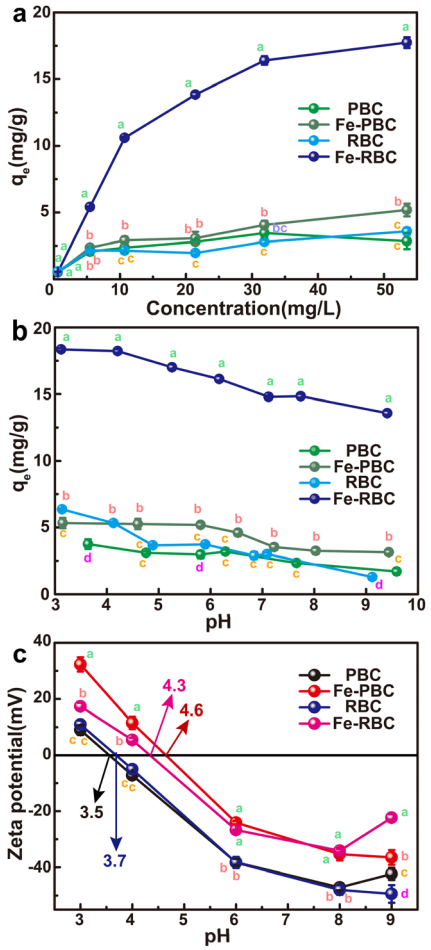

Fig. 6 Effect of (a) initial MO concentration and (b) pH on MO removal in all systems. (c) Zeta potential of biochar samples at different pH. Biochar dose = 1.0 g L^{-1}, $[MO]_0$ = 20 mg L^{-1}, and T = 25 °C. Lower letters (a, b, c, d) indicate significant differences in adsorption physical and chemical properties between different biochar ($p < 0.05$).

SO_3) and amine ($-N(CH_3)_2$) groups with pK_a value of 3.8. In the solution with a lower pH of 3.8, the MO molecules existed in zwitterion form, with protonated amine groups and negatively charged sulfonated groups. At pH levels above 3.8, the amine groups began to deprotonate, while the negative charge density of the sulfonate groups increased significantly. Consequently, MO molecules carried a negative charge under these conditions. Moreover, the pH_{pzc} value of biochar samples was varying from 3.5 to 4.6 ($p < 0.05$) in Fig. 6c. Thus, the biochar surface was positively charged at a solution pH of 3.5 and below. Under acidic conditions, the MO molecules became negative and caused the electrostatic attraction between adsorbate and adsorbent, which was beneficial to the adsorption of MO. It is noteworthy that iron loading can enhance the surface charge density of biochar, particularly in Fe-PBC, thereby reducing electrostatic repulsion between MO and biochar. This improvement likely contributes to the effective MO adsorption by iron-supported biochar. Additionally, iron loading may introduce new adsorption sites on the biochar surface, effectively capturing MO molecules. Overall, the iron/biochar samples demonstrated good immobilization performance across a wide range of pH values ($p < 0.05$), highlighting their potential for application in various environment.

3.4 Adsorption mechanism

The biochar samples were re-examined using FT-IR and XPS spectra before and after MO adsorption to investigate the mechanism of MO removal. Fig. 7a and b showed that the peak intensity of N 1s significantly increased after MO adsorption, which indicates that MO was successfully immobilized on the adsorbent.[49] Fig. 7c showed the changes in surface functional groups before and after MO adsorption on iron/biochar samples. It was evident that after MO adsorption, the peak positions of C–O, C=O, Fe–O, and Si–OH shifted slightly, indicating the involvement of these functional groups in the adsorption process. This phenomenon can be explained by π–π interactions, where the C=C and C=O functional groups on the biochar surface act as π-electron donors, binding to MO.[49,63] It was noteworthy that the peak position of OH was significantly enhanced after adsorption, attributed to the formation of hydrogen bonds between the molecular structures of MO and Fe-RBC, such as the N atoms in MO forming hydrogen bonds with –OH on the surface of biochar.[64] Furthermore, the functional group of –S=O in MO molecule could also form hydrogen bonds with the –OH group on the Fe-PBC and Fe-RBC surface during the adsorption process.[49,65]

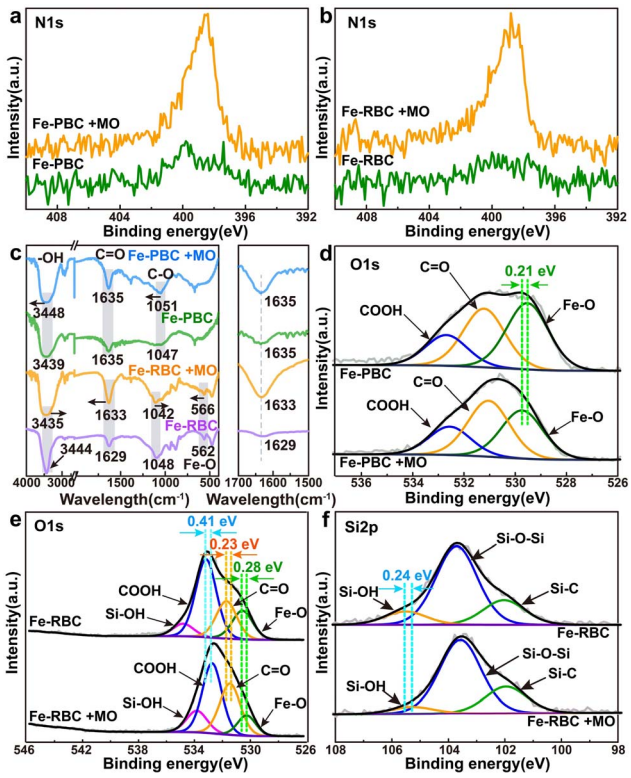

Fig. 7 High-resolution of N 1s XPS spectra of (a) Fe-PBC and (b) Fe-RBC, FT-IR spectra (c) of Fe-PBC and Fe-RBC, O 1s XPS spectra of (d) Fe-PBC and (e) Fe-RBC, (f) Si 2p of Fe-RBC before and after the adsorption of MO.

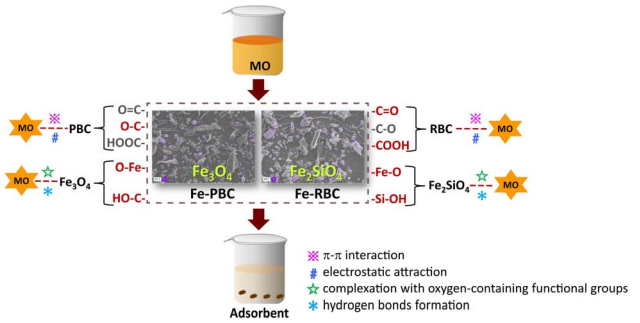

Fig. 8 Proposed mechanisms of Fe-PBC and Fe-RBC adsorbed MO.

As shown in the XPS spectra of C 1s, O 1s, and Si 2p, the binding energies of Fe–O, C=O, and COOH shifted to lower positions after MO adsorption onto the iron/biochar surface (Fig. 7d and e). However, the binding energy of Si–O in Fe-RBC increased to higher positions (Fig. 7f). The coordination between metal and oxygen functionalities was also considered as a key mechanism for MO adsorption on biochar.[45,66] These results suggested a synergistic effect between the iron-containing minerals formed on the surface of the iron/biochar and the biochar itself during MO adsorption. Based on the above results, the mechanisms of MO adsorption on the surface of iron/biochar were summarized in Fig. 8. MO in the solution quickly reached the surface of iron/biochar *via* intra-particle diffusion and was then adsorbed by the iron particles (Fe–O, Si–O) and biochar substrates (C=O, COOH, OH) through electrostatic attraction. By comparison, Fe-RBC had more adsorption sites than Fe-PBC, as confirmed by the adsorption experiment results.

3.5 The reusability of biochar

The reusability of all biochar samples and MO desorption was investigated by a three-run cycle test. We used neutral deionized water as an eluent to remove the deposited MO molecules. After adsorption equilibrium was obtained, biochar samples were collected and washed with 50 mL deionized water to remove the deposited MO. Afterward, the biochar samples were dried at 60 °C for 6 h for the next cycle. As shown in Fig. 9, the ratio of adsorbed MO by Fe-PBC and Fe-RBC in water decreased from 73% and 21% to 11% and 2% after three cycle runs. The results suggest a poor reusability for biochar samples, which can be attributed to the incomplete elution of MO. The occupied adsorption sites lead to a decline in the adsorption cycle of MO for biochar samples.

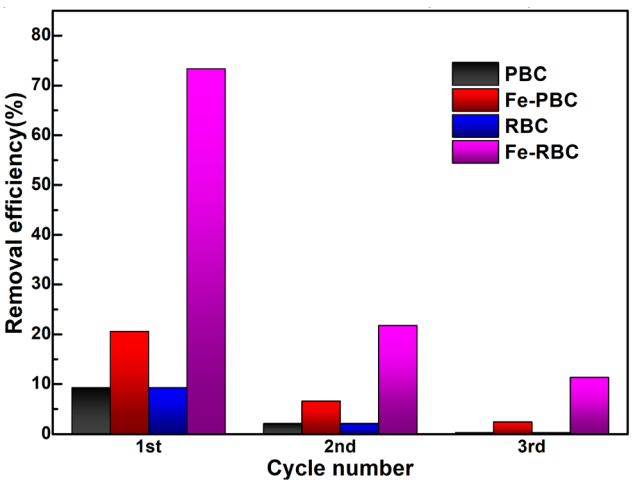

Fig. 9 The reusability tests of all biochar samples.

4 Conclusion

In this study, two types of biochar loaded with iron-containing minerals were successfully prepared by pyrolyzing different impregnated biomasses with Fe^{3+}. The influence of different biomass on the structure and adsorption mechanism of MO was investigated. Differences in biomass led to the formation of various iron-bearing minerals on the surface of biochar, with peanut shell biochar producing Fe_3O_4 and rice husk biochar producing Fe_2SiO_4 on the surface. The introduction of iron-containing minerals not only increased the surface areas and pore structure, but also introduced abundant adsorption sites of biochar. The adsorption of MO by the four biochar was in the order: Fe-RBC (17.2 mg g^{-1}) ≫ Fe-PBC (6.0 mg g^{-1}) > RBC (4.5 mg g^{-1}) > PBC (3.9 mg g^{-1}). Through characterization and experimental tests, it is demonstrated that the mechanisms responsible for MO immobilization on the iron/biochar surface involved four pathways: electrostatic attraction, complexation with oxygen-containing functional groups, π–π interaction and hydrogen bonds formation. Moreover, differences in the mineral species on iron/biochar surface led to very different adsorption sites. This study showed a synergistic effect between the iron-containing minerals formed on the surface of the iron/biochar and the biochar itself during MO adsorption. Additionally, this study also provided insights for selecting biochar adsorbents to remove MO pollutants in environmental systems and serves as an example of the microscopic interaction mechanisms between MO and carbon-based adsorbents.

Data availability

Data will be made available on request.

Author contributions

Yaqiong Dong: conceptualization, data curation, formal analysis, investigation, methodology, writing-original draft. Jianjun Liang: writing-review & editing, supervision. Zhengyang E: data curation and validation. Jiayu Song: data curation and validation. Changjie Liu: writing-review & editing, funding acquisition. Zhe Ding: data curation and validation, supervision. Wei Wang: data curation and validation. Wentao Zhang: writing-reviewing & editing, funding acquisition.

Conflicts of interest

There are no conflicts to declare.

Acknowledgements

This study was financially supported by the National Natural Science Foundation of China (42302190), "100-Talent" program from Chinese Academy of Sciences and Natural Science Foundation of Gansu Province (Grant No. 22JR5RA092).

Notes and references

1 G. Huang, X. Su, M. S. Rizwan, *et al.*, Chemical immobilization of Pb, Cu, and Cd by phosphate materials and calcium carbonate in contaminated soils, *Environ. Sci. Pollut. Res.*, 2016, **23**, 16845–16856.

2 C. Zhang, L. Liu, M. Zhao, *et al.*, The environmental characteristics and applications of biochar, *Environ. Sci. Pollut. Res.*, 2018, **25**, 21525–21534.

3 G. Akgul, T. B. Maden, E. Diaz, *et al.*, Modification of tea biochar with Mg, Fe, Mn and Al salts for efficient sorption of PO_4^{3-} and Cd^{2+} from aqueous solutions, *J. Water Reuse Desalin.*, 2018, **9**, 57–66.

4 L. Liu, X. Yang, S. Ahmad, *et al.*, Silicon (Si) modification of biochars from different Si-bearing precursors improves cadmium remediation, *Chem. Eng. J.*, 2023, **457**, 141194.

5 J. Yu, L. Tang, Y. Pang, *et al.*, Magnetic nitrogen-doped sludge-derived biochar catalysts for persulfate activation: internal electron transfer mechanism, *Chem. Eng. J.*, 2019, **364**, 146–159.

6 B. Yao, Z. Luo, J. Yang, *et al.*, Fe^{II} Fe^{III} layered double hydroxide modified carbon felt cathode for removal of ciprofloxacin in electro-Fenton process, *Environ. Res.*, 2021, **197**, 111144.

7 F. Ameen, R. Mostafazadeh, Y. Hamidian, *et al.*, Modeling of adsorptive removal of azithromycin from aquatic media by $CoFe_2O_4$/NiO anchored microalgae-derived nitrogen-doped porous activated carbon adsorbent and colorimetric quantifying of azithromycin in pharmaceutical products, *Chemosphere*, 2023, **329**, 138635.

8 G. Abdul, X. Zhu and B. Chen, Structural characteristics of biochar-graphene nanosheet composites and their adsorption performance for phthalic acid esters, *Chem. Eng. J.*, 2017, **319**, 9–20.

9 J. Kanjanarong, B. S. Giri, D. P. Jaisi, *et al.*, Removal of hydrogen sulfide generated during anaerobic treatment of sulfate-laden wastewater using biochar: evaluation of efficiency and mechanisms, *Bioresour. Technol.*, 2017, **234**, 115–121.

10 C. Chen, F. Yang, Y. Ma, *et al.*, Ball milling boosted magnetic cotton husk-derived biochar adsorptive removal of oxytetracycline and ciprofloxacin from water, *Carbon Res.*, 2024, **3**, 63.

11 D. Woolf, J. E. Amonette, F. A. Street-Perrott, *et al.*, Sustainable biochar to mitigate global climate change, *Nat. Commun.*, 2010, **1**, 56.

12 C. J. Atkinson, How good is the evidence that soil-applied biochar improves water-holding capacity?, *Soil Use Manage.*, 2018, **34**, 177–186.

13 P. Liu, W.-J. Liu, H. Jiang, *et al.*, Modification of bio-char derived from fast pyrolysis of biomass and its application in removal of tetracycline from aqueous solution, *Bioresour. Technol.*, 2012, **121**, 235–240.

14 M. B. Ahmed, J. L. Zhou, H. H. Ngo, *et al.*, Sorption of hydrophobic organic contaminants on functionalized biochar: protagonist role of π–π electron–donor–acceptor interactions and hydrogen bonds, *J. Hazard. Mater.*, 2018, **360**, 270–278.

15 M. Ahmad, A. U. Rajapaksha, J. E. Lim, *et al.*, Biochar as a sorbent for contaminant management in soil and water: a review, *Chemosphere*, 2014, **99**, 19–33.

16 K. S. D. Premarathna, A. U. Rajapaksha, B. Sarkar, *et al.*, Biochar-based engineered composites for sorptive decontamination of water: a review, *Chem. Eng. J.*, 2019, **372**, 536–550.

17 S. Wang, M. Zhao, M. Zhou, *et al.*, Biochar-supported nZVI (nZVI/BC) for contaminant removal from soil and water: a critical review, *J. Hazard. Mater.*, 2019, **373**, 820–834.

18 A. U. Rajapaksha, S. S. Chen, D. C. W. Tsang, *et al.*, Engineered/designer biochar for contaminant removal/immobilization from soil and water: potential and implication of biochar modification, *Chemosphere*, 2016, **148**, 276–291.

19 D.-W. Cho, K. Yoon, Y. Ahn, *et al.*, Fabrication and environmental applications of multifunctional mixed metal-biochar composites (MMBC) from red mud and lignin wastes, *J. Hazard. Mater.*, 2019, **374**, 412–419.

20 Y. Sun, I. K. M. Yu, D. C. W. Tsang, *et al.*, Multifunctional iron-biochar composites for the removal of potentially toxic elements, inherent cations, and hetero-chloride from hydraulic fracturing wastewater, *Environ. Int.*, 2019, **124**, 521–532.

21 K. S. D. Premarathna, A. U. Rajapaksha, N. Adassoriya, *et al.*, Clay-biochar composites for sorptive removal of tetracycline antibiotic in aqueous media, *J. Environ. Manage.*, 2019, **238**, 315–322.

22 O. Sahin, M. B. Taskin, E. C. Kaya, *et al.*, Effect of acid modification of biochar on nutrient availability and maize growth in a calcareous soil, *Soil Use Manage.*, 2017, **33**, 447–456.

23 S. Sugashini and K. M. M. S. Begum, Performance of Fe-loaded chitosan carbonized rice husk beads (Fe-CCRB) for continuous adsorption of metal ions from industrial effluents, *Environ. Prog. Sustain.*, 2014, **33**, 1125–1138.

24 A. Ayati, B. Tanhaei, H. Beiki, *et al.*, Insight into the adsorptive removal of ibuprofen using porous carbonaceous materials: a review, *Chemosphere*, 2023, **323**, 138241.

25 T. E. Rufford, D. Hulicova-Jurcakova, Z. Zhu, *et al.*, A comparative study of chemical treatment by $FeCl_3$, $MgCl_2$, and $ZnCl_2$ on microstructure, surface chemistry, and double-layer capacitance of carbons from waste biomass, *J. Mater. Res.*, 2010, **25**, 1451–1459.

26 J. Kim, J. Song, S.-M. Lee, *et al.*, Application of iron-modified biochar for arsenite removal and toxicity reduction, *J. Ind. Eng. Chem.*, 2019, **80**, 17–22.

27 Z. Song, Y. Liu, L. Liu, *et al.*, Reusable magnetically-modified enteromorpha prolifera-based biochar hydrogels: competitive removal mechanism for metal-organic dye composite contaminants, *Carbon Res.*, 2024, **3**, 18.
28 S. Guo, J. Zhang, X. Li, *et al.*, Fe_3O_4-CS-L: a magnetic core-shell nano adsorbent for highly efficient methyl orange adsorption, *Water Sci. Technol.*, 2017, **77**, 628–637.
29 X. Zhang, Y. Li, G. Li, *et al.*, Preparation of Fe/activated carbon directly from rice husk pyrolytic carbon and its application in catalytic hydroxylation of phenol, *RSC Adv.*, 2015, **5**, 4984–4992.
30 P. Zhang, D. O'Connor, Y. Wang, *et al.*, A green biochar/iron oxide composite for methylene blue removal, *J. Hazard. Mater.*, 2020, **384**, 121286.
31 S. Wang, B. Gao, A. R. Zimmerman, *et al.*, Removal of arsenic by magnetic biochar prepared from pinewood and natural hematite, *Bioresour. Technol.*, 2015, **175**, 391–395.
32 L. Luo, C. Xu, Z. Chen, *et al.*, Properties of biomass-derived biochars: combined effects of operating conditions and biomass types, *Bioresour. Technol.*, 2015, **192**, 83–89.
33 S. Wang, B. Gao, A. R. Zimmerman, *et al.*, Physicochemical and sorptive properties of biochars derived from woody and herbaceous biomass, *Chemosphere*, 2015, **134**, 257–262.
34 D. Aran, J. Antelo, S. Fiol, *et al.*, Influence of feedstock on the copper removal capacity of waste-derived biochars, *Bioresour. Technol.*, 2016, **212**, 199–206.
35 Y. Yang, K. Sun, L. Han, *et al.*, Effect of minerals on the stability of biochar, *Chemosphere*, 2018, **204**, 310–317.
36 S. S. Mayakaduwa, I. Herath, Y. S. Ok, *et al.*, Insights into aqueous carbofuran removal by modified and non-modified rice husk biochars, *Environ. Sci. Pollut. Res.*, 2017, **24**, 22755–22763.
37 Q. Zhang, Z. Yang and W. Wu, Role of Crop Residue Management in Sustainable Agricultural Development in the North China Plain, *J. Sustain. Agr.*, 2008, **32**, 137–148.
38 P. Yuan, D. Liu, M. Fan, *et al.*, Removal of hexavalent chromium [Cr(VI)] from aqueous solutions by the diatomite-supported/unsupported magnetite nanoparticles, *J. Hazard. Mater.*, 2010, **173**, 614–621.
39 B.-S. Trinh, P. T. K. Le, D. Werner, *et al.*, Rice Husk Biochars Modified with Magnetized Iron Oxides and Nano Zero Valent Iron for Decolorization of Dyeing Wastewater, *Processes*, 2019, **7**, 660.
40 B. Kayranli, Cadmium removal mechanisms from aqueous solution by using recycled lignocelluloses, *Alex. Eng. J.*, 2022, **61**, 443–457.
41 K. O. Iwuozor, J. O. Ighalo, E. C. Emenike, *et al.*, Adsorption of methyl orange: a review on adsorbent performance, *Curr. Res. Green Sustainable Chem.*, 2021, **4**, 100179.
42 P. A. Soares, T. F. C. V. Silva, D. R. Manenti, *et al.*, Insights into real cotton-textile dyeing wastewater treatment using solar advanced oxidation processes, *Environ. Sci. Pollut. Res.*, 2014, **21**, 932–945.
43 H. Lyu, J. Tang, M. Cui, *et al.*, Biochar/iron (BC/Fe) composites for soil and groundwater remediation: synthesis, applications, and mechanisms, *Chemosphere*, 2020, **246**, 125609.
44 S. Zeng, Y.-K. Choi and E. Kan, Iron-activated bermudagrass-derived biochar for adsorption of aqueous sulfamethoxazole: effects of iron impregnation ratio on biochar properties, adsorption, and regeneration, *Sci. Total Environ.*, 2021, **750**, 141691.
45 H. Cheng, Y. Liu and X. Li, Adsorption performance and mechanism of iron-loaded biochar to methyl orange in the presence of Cr^{6+} from dye wastewater, *J. Hazard. Mater.*, 2021, **415**, 125749.
46 X. Zhu, F. Qian, Y. Liu, *et al.*, Controllable synthesis of magnetic carbon composites with high porosity and strong acid resistance from hydrochar for efficient removal of organic pollutants: an overlooked influence, *Carbon*, 2016, **99**, 338–347.
47 I. Akin, G. Arslan, A. Tor, *et al.*, Arsenic(V) removal from underground water by magnetic nanoparticles synthesized from waste red mud, *J. Hazard. Mater.*, 2012, **235–236**, 62–68.
48 W.-T. Tan, H. Zhou, S.-F. Tang, *et al.*, Enhancing Cd(II) adsorption on rice straw biochar by modification of iron and manganese oxides, *Environ. Pollut.*, 2022, **300**, 118899.
49 J. Wang, W. Chen, M. Zhang, *et al.*, Optimize the preparation of Fe_3O_4-modified magnetic mesoporous biochar and its removal of methyl orange in wastewater, *Environ. Monit. Assess.*, 2021, **193**, 1–20.
50 Z. Wang, B. Peng, L. Zhang, *et al.*, Study on Formation Mechanism of Fayalite (Fe_2SiO_4) by Solid State Reaction in Sintering Process, *JOM*, 2018, **70**, 539–546.
51 P. J. M. Carrott, M. M. L. Ribeiro Carrott and Suhas, Comparison of the Dubinin–Radushkevich and Quenched Solid Density Functional Theory approaches for the characterisation of narrow microporosity in activated carbons obtained by chemical activation with KOH or NaOH of Kraft and hydrolytic lignins, *Carbon*, 2010, **48**, 4162–4169.
52 A. V. Maldhure and J. D. Ekhe, Preparation and characterizations of microwave assisted activated carbons from industrial waste lignin for Cu(II) sorption, *Chem. Eng. J.*, 2011, **168**, 1103–1111.
53 A. Dąbrowski, Adsorption—from theory to practice, *Adv. Colloid Interface Sci.*, 2001, **93**, 135–224.
54 M. S. Mel'gunov, Application of the simple Bayesian classifier for the N_2 (77 K) adsorption/desorption hysteresis loop recognition, *Adsorption*, 2023, **29**, 199–208.
55 O. Üner and Y. Bayrak, The effect of carbonization temperature, carbonization time and impregnation ratio on the properties of activated carbon produced from Arundo donax, *Micropor. Mesopor. Mater.*, 2018, **268**, 225–234.
56 J. Wang, W. Chen, M. Zhang, *et al.*, Optimize the preparation of Fe_3O_4-modified magnetic mesoporous biochar and its removal of methyl orange in wastewater, *Environ. Monit. Assess.*, 2021, **193**, 179.
57 F. Liu, J. Zuo, T. Chi, *et al.*, Removing phosphorus from aqueous solutions by using iron-modified corn straw biochar, *Front. Env. Sci. Eng.*, 2015, **9**, 1066–1075.
58 K. C. Bedin, A. C. Martins, A. L. Cazetta, *et al.*, KOH-activated carbon prepared from sucrose spherical carbon: adsorption

equilibrium, kinetic and thermodynamic studies for Methylene Blue removal, *Chem. Eng. J.*, 2016, **286**, 476–484.

59 C.-H. Liu, Y.-H. Chuang, H. Li, *et al.*, Long-term sorption of lincomycin to biochars: the intertwined roles of pore diffusion and dissolved organic carbon, *Water Res.*, 2019, **161**, 108–118.

60 M. Inyang, B. Gao, A. Zimmerman, *et al.*, Synthesis, characterization, and dye sorption ability of carbon nanotube–biochar nanocomposites, *Chem. Eng. J.*, 2014, **236**, 39–46.

61 B. Xiao, Q. Dai, X. Yu, *et al.*, Effects of sludge thermal-alkaline pretreatment on cationic red X-GRL adsorption onto pyrolysis biochar of sewage sludge, *J. Hazard. Mater.*, 2018, **343**, 347–355.

62 N. Tabassam, S. Mutahir, M. A. Khan, *et al.*, Facile synthesis of cinnamic acid sensitized rice husk biochar for removal of organic dyes from wastewaters: Batch experimental and theoretical studies, *Mater. Chem. Phys.*, 2022, **288**, 126327.

63 J. Luo, X. Li, C. Ge, *et al.*, Preparation of ammonium-modified cassava waste-derived biochar and its evaluation for synergistic adsorption of ternary antibiotics from aqueous solution, *J. Environ. Manage.*, 2021, **298**, 113530.

64 A.-T. Mohammad, A. S. Abdulhameed and A. H. Jawad, Box-Behnken design to optimize the synthesis of new crosslinked chitosan-glyoxal/TiO_2 nanocomposite: methyl orange adsorption and mechanism studies, *Int. J. Biol. Macromol.*, 2019, **129**, 98–109.

65 N. Chaukura, E. C. Murimba and W. Gwenzi, Synthesis, characterisation and methyl orange adsorption capacity of ferric oxide-biochar nano-composites derived from pulp and paper sludge, *Appl. Water Sci.*, 2017, **7**, 2175–2186.

66 P. Wu, P. Cui, Y. Zhang, *et al.*, Unraveling the molecular mechanisms of Cd sorption onto MnOx-loaded biochar produced from the Mn-hyperaccumulator Phytolacca americana, *J. Hazard. Mater.*, 2022, **423**, 127157.